

# The Bullet Cluster revisited: New results from new constraints and improved strong lensing modeling technique

D. Paraficz<sup>1</sup>, J.-P. Kneib<sup>1</sup>, J. Richard<sup>2,3</sup>, A. Morandi<sup>4</sup>, M. Limousin<sup>1,2</sup>, E. Jullo<sup>1</sup>

<sup>1</sup>*Aix Marseille University, CNRS, LAM (Laboratoire d'Astrophysique de Marseille) UMR 7326, 13388, Marseille, France*

<sup>2</sup>*Dark Cosmology Centre, Niels Bohr Institute, University of Copenhagen, Juliane Maries Vej 30, DK-2100 Copenhagen, Denmark*

<sup>3</sup>*CRAL, Observatoire de Lyon, Université Lyon 1, 9 Avenue Ch. Andr e, 69561 Saint Genis Laval Cedex, France*

<sup>4</sup>*Raymond and Beverly Sackler School of Physics and Astronomy, Tel Aviv University, Tel Aviv, 69978, Israel*

27 June 2022

## ABSTRACT

We present a new detailed parametric strong lensing mass reconstruction of the “Bullet Cluster” (1E 0657-56) at  $z=0.296$ , based on new WFC3 and ACS HST imaging and VLT/FORS2 spectroscopy. The strong lensing constraints undergone deep revision, there are 14 (6 new and 8 previously known) multiply imaged systems, of which 3 have spectroscopically confirmed redshifts (including 2 newly measured). The reconstructed mass distribution includes explicitly for the first time the combination of 3 mass components: *i*) the intra-cluster gas mass derived from X-ray observation, *ii*) the cluster galaxies modeled by their Fundamental Plane (elliptical) and Tully-Fisher (spiral) scaling relations and *iii*) dark matter. The best model has an average rms value of  $0.158''$  between the predicted and measured image positions for the 14 multiple images considered. The derived mass model confirms the spacial offset between the X-ray gas and dark matter peaks. The galaxy halos to total mass fraction is found to be  $f_s = 11 \pm 5\%$  for a total mass of  $2.5 \pm 0.1 \times 10^{14} M_\odot$  within a 250 kpc radial aperture.

## Key words:

gravitational lensing; strong, galaxies: clusters: individual: Bullet Cluster

## 1 INTRODUCTION

The massive galaxy cluster, 1E 0657-56, discovered by Tucker et al. (1998) consists of two colliding galaxy clusters at  $z = 0.296$ . In this distinct merging system, a sub-cluster, the “bullet” has collided with the main cluster, approximately in the plane of the sky (Barrena et al. 2002). The bullet-like sub-cluster has produced strong bow shock in the intra-cluster gas during the collision and consequently the collision striped the gas from the cluster potential (Markevitch et al. 2002). The offset between the two baryonic components (gas and galaxies) gave a unique possibility for the indirect measurements of the total mass distribution using gravitational lensing studies (Mehlert et al. 2001; Clowe et al. 2004; Brada c et al. 2006, 2009), which unambiguously demonstrated that dark matter (DM) traces the collisionless galaxies and not the X-ray gas. The study of the lensing mass distribution of the Bullet Cluster remains a powerful evidence of the DM existence that severely challenges the theory of modified gravity such as MOND and TeVeS (Milgrom 1983; Bekenstein 2004). It also gives upper limits on

the DM self interaction cross section (Randall et al. 2008; Markevitch et al. 2004) and lower limit on the possible radiative decay of DM (Boyarsky et al. 2008).

Since the first lensing mass measurement of the Bullet Cluster considerable effort has been put in constraining its mass distribution. Nevertheless, significant discrepancies exist, e.g. the mass derived from the Clowe et al. (2004) and Brada c et al. (2006) differ by a factor 2. Although, this is likely due to degeneracies of lens modeling between strong and weak lensing mass estimates, the Brada c et al. (2006) mass measurement uncertainty is still as high as 14% over the full ACS field. Indeed, the complexity of the Bullet Cluster and the limited number of multiple images makes its strong lens modeling exceptionally challenging. The way forward to improve the mass modeling is to use more constraints either coming from the lensing or from other techniques (e.g. X-ray). As witnessed in other clusters (e.g. Abell 1689, 1703, 2218, see Richard et al. 2010b), the accuracy of the lensing mass map is strongly dependent on the correct identification and on the number of multiply imaged systems used to constrain it. Hence, to construct a robust mass

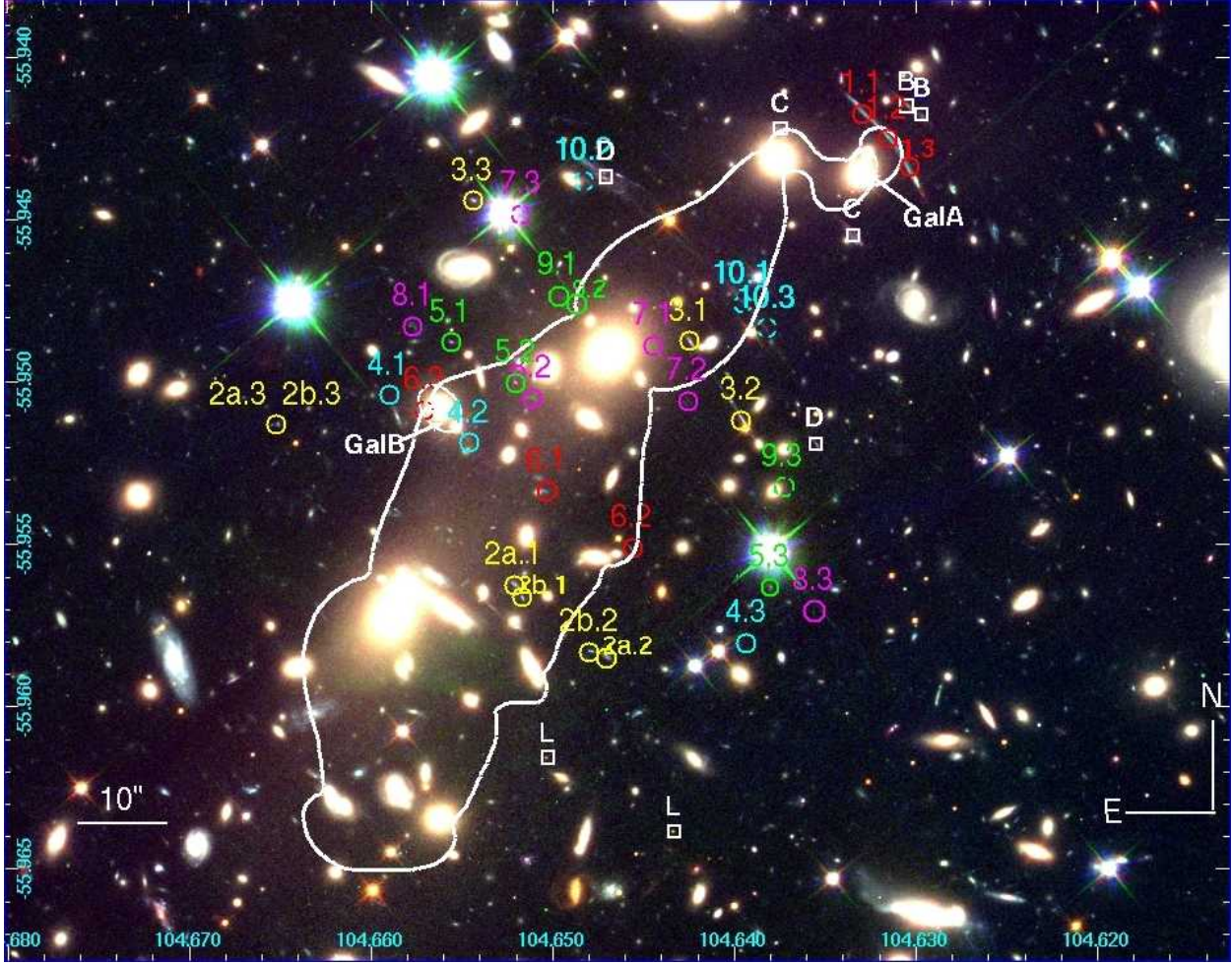


**Figure 1.** Colour HST image of the main cluster component of 1E 0657-56 (blue–F606W, green–F814W, red–F160W). Multiple images considered in this work are marked with colour circles (dashed line circles mark the predicted but not confirmed positions of counter images), the spectroscopically confirmed multiply imaged systems are 1 and 4. White squares are referring to (Bradač et al. 2006) systems, which we have not included in our modeling. System 10 (cyan dashed circles) is a multiple imaged candidate and is not a part of model constraints due to extended morphology and the large uncertainty in locating the different multiple image centers. The white line represent a critical line corresponding to  $z = 3.24$ .

model it is important to include as many spectroscopically *confirmed* multiply imaged systems as possible.

In this work we present an improved high-resolution mass model of the Bullet Cluster based on the identification of new multiple imaged systems and new spectroscopic redshifts measurements of the strongly lensed background galaxies. These results are based on new and archival Advanced Camera for Surveys (ACS) images and new Wide Field Camera 3 (WFC3) images as well as on new spectroscopic redshift determination of multiply imaged systems, one taken from the literature and one obtained through VLT/FORS2 observations. Furthermore, the mass distribution reconstructed includes for the first time the combination of the following mass components: *i*) the intra-cluster gas mass derived from X-ray observation, *ii*) the cluster galaxies modeled by their Fundamental Plane (elliptical) and Tully-Fisher (spiral) scaling relations and *iii*) dark matter. The gas mass component is distinctive in the Bullet Cluster since the gas is spatially shifted from the main mass component of the cluster ( $\sim 47''$  Clowe et al. 2006) and has been thoroughly

studied. Nevertheless, until now the gas component of the cluster has not been independently taken into account in any of the lens modeling. Enriching our modeling technique and improving the lensing constraints allowed us to create a more accurate mass model with significantly smaller systematic uncertainties.

This paper is structured as follows. Section 2 describes the data and its reduction procedures. Section 3 describes the previous achievements in the field and presents our multiply imaged systems. Section 4 presents the method of mass reconstruction of the Bullet Cluster, describes newly implemented mass modeling improvements (new scaling relations and X-rays mass map). Our conclusions are summarized in Section 5

Throughout the paper, we assume a  $\Lambda$  Cold Dark Matter ( $\Lambda$ CDM) cosmology with  $\Omega_m = 0.3$ ,  $\Omega_\Lambda = 0.7$  and  $h = 0.7$ . At the cluster redshift ( $z = 0.296$ )  $1''$  corresponds to 4.413 kpc.

All the figures of the cluster are aligned with WCS coordinates, i.e., North is up, East is left. The reference center



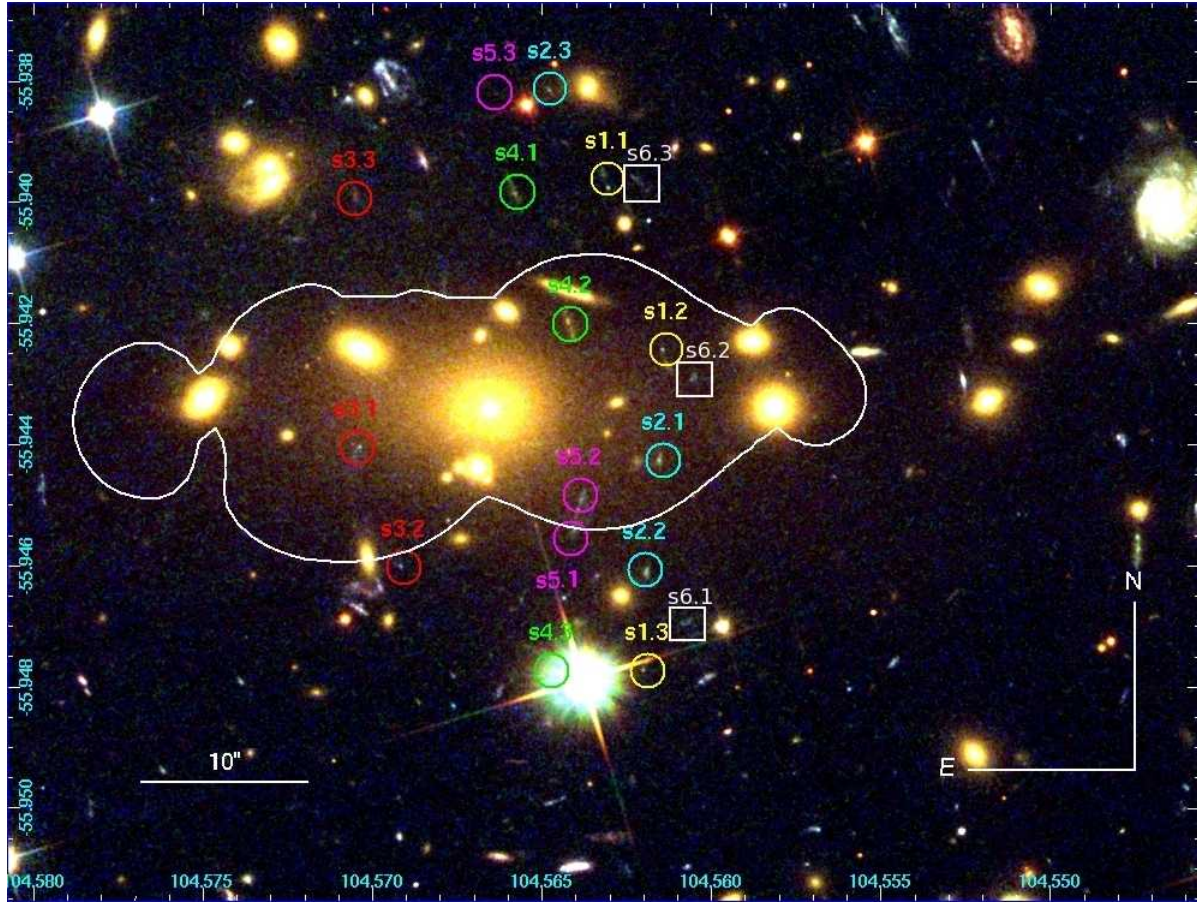


**Figure 2.** Colour ACS/HST image of the sub cluster component of 1E 0657-56 (blue–F435W, green–F606W, red–F814W). Multiple images considered in this work are marked with colour circles, the spectroscopically confirmed multiply imaged system is system marked as s1. System s6 (white squares) is a multiple imaged candidate and is not a part of model constraints due to large colour uncertainties. The white line represent a critical line corresponding to  $z = 2.99$ .

of our analysis is fixed at the BCG 1 center:  $\alpha = 104.6588589$ ,  $\delta = -55.9571863$  (J2000.0). Magnitudes are given in the AB system. All uncertainties and upper/lower limits are stated and/or plotted at  $1\sigma$  confidence.

## 2 OBSERVATIONS AND DATA REDUCTION

### 2.1 Hubble imaging

The first round of observation of the cluster 1E 0657-56 with the Hubble Space Telescope (HST) was carried out between 2004 and 2006 using the ACS camera (HST programs 10200 and 10863, PI: Jones & Gonzalez) at two side-by-side positions covering the main cluster and the Western sub-cluster. The main cluster was observed in F606W, F775W and F850LP bands (hereafter V,i,z), and the sub-cluster in F435W, F606W, F814W (hereafter B,V,I) (see Figure 1 and 2). The F606W band covering both components is used for a uniform view of the cluster, as well as detections in the photometric catalog. Details on the exposure times and quality of these data have been presented in Bradač et al. (2009).

In addition, HST/WFC3 imaging has been performed in F110W and F160W filters, with two largely overlapping

positions centered on the main cluster (PID: 11099; PI: Bradac), and with a single pointing at the center of the main cluster (PID:11591; PI: Kneib). The total exposure time in F110W/F160W was 6529/7029 secs for the first program, and 3211/2811 secs for the second program, with 9740/9840 secs in the overlapping region, making it one of the deepest WFC3 images on a lensing cluster. The magnitude limits at  $3 - \sigma$  measured using  $0.25''$  radius aperture the deepest data reach 28.76 and 28.15 in F110W and F160W band, respectively.

Finally, in February 2011, the main cluster of 1E 0657-56 was observed with the ACS camera using the F814W filter as part of the programme 11591. The total exposure time was 4480 secs (2 orbits).

Both ACS and WFC3 data have been aligned using the multidrizzle (Koekemoer et al. 2002) software, including some relative shifts measured with IRAF for datasets taken at different epochs. The F606W image was used for overall alignment of the different bands, and the USNO catalog provided accurate astrometric calibration.

We use the double-image mode (with F606W being a detection image) of the SEXTRACTOR package (Bertin & Arnouts 1996) to detect objects and compute magnitudes within a  $0.5''$  diameter aperture (ACS images). Corrections to total magnitudes, to account for the flux falling outside of

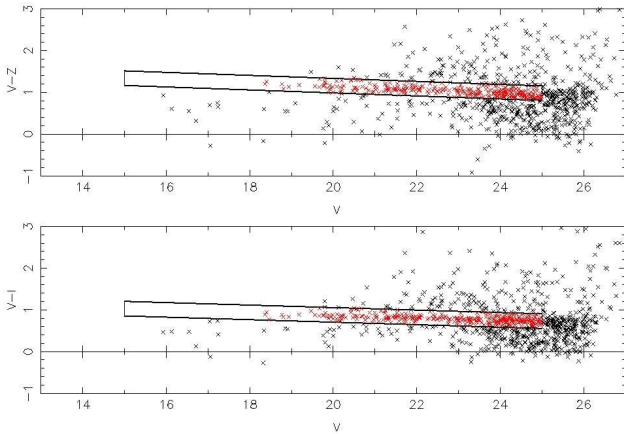


**Figure 3.** Colour-magnitude diagrams and the selection of cluster member galaxies. The red sequence selection is shown in the black boxes: all galaxies in this box are considered to be cluster galaxies. [(V-I) vs. V] or [(V-z) vs. V] colour-magnitude diagrams correspond to the main and sub-cluster components, respectively.

the aperture, were estimated using bright isolated unsaturated stars. The corresponding values are 0.25 for WFC3 and 0.1 mag for ACS. All of our imaging data (optical/ACS and near-IR/WFC3) are PSF-matched to the WFC3/IR F160W imaging data before making colour measurements. We measure isophotal magnitudes to produce accurate colors and photometric redshifts.

The half-light radius  $R_e$  used in the Fundamental Plane galaxy scaling was measured using the SEXTRACTOR (FLUX\_RADIUS) on F606W image. Considering the large amount of cluster members the automated approach of SEXTRACTOR was chosen over the precision that would be given by dedicated but more complex softwares such as GALFIT.

## 2.2 Cluster member identification

Cluster galaxies were identified based on the ACS data using the characteristic cluster red-sequences identified using the [(V-I) vs. V] or [(V-z) vs. V] colour-magnitude diagrams (see Figure 3), for the main and sub-cluster components, respectively. The galaxies lying in both red sequences were assumed to be cluster members. In order to save computing time we have included in the lens modeling only the 100 brightest cluster galaxies ( $V < 25.2$ ), that roughly corresponds to lensing deflection larger than  $\sim 0.1''$ ).

## 2.3 VLT/FORS2 spectroscopy

We have used the FOCAL Reducer and low dispersion Spectrograph (FORS2, Appenzeller et al. (1998)) at the Very Large Telescope to measure the spectroscopic redshift of multiply imaged systems. MXU masks with  $1''$ -wide slits were designed to cover most of the multiple images identified in the Bullet Cluster. Observations were obtained on the 3 nights of February 15-17th 2010, with a total of 9.9 kssec split into 900 seconds exposures. The G300V grism and the GG435 order-sorting filter were used to provide a good coverage of the reddest wavelengths ( $4450 < \lambda < 8650 \text{ \AA}$ ) a dispersion of  $2.69 \text{ \AA}$  per pixel and a resolution  $R = \lambda/\Delta\lambda \sim 200$

at the central wavelength  $5900 \text{ \AA}$ . Standard stars were observed during the same nights, and the data reduction was performed with a combination of the ESOREX package and standard IRAF routines to improve the sky subtraction and wavelength calibration of specific slits.

Within these shallow spectroscopic data we only manage to measure the redshift for two systems. We confirm the  $z=3.24$  spectroscopic redshift of System 1, previously found by Mehlert et al. (2001). We also measured the redshift of s1, one of the multiply imaged systems identified in the sub-cluster. This source shows a strong emission line at  $4851 \text{ \AA}$  which we interpret as Lyman- $\alpha$  at  $z = 2.99$  from the lensing configuration and the lack of additional emission lines. The other likely alternative is [OII], observed at  $4851 \text{ \AA}$  would give a redshift of 0.301, similar to the cluster redshift, thus the alternative can be excluded.

## 3 MULTIPLE-IMAGE IDENTIFICATION

### 3.1 Previous work

The first lens model of the Bullet Cluster, derived by Mehlert et al. (2001) was based on 3 parametrically modeled DM clumps and 150 cluster members modeled using the Faber-Jackson relation (Faber & Jackson 1976). As lensing constraints Mehlert et al. (2001) used 6 multiply imaged system (labeled A to F selected from deep BgRI VLT/FORS images) of which one of them (the giant arc) they measured a spectroscopic redshift of  $z = 3.24$ .

Bradač et al. (2006, 2009) applied a non-parametric mass reconstruction method based on strong and weak gravitational lensing (their weak lensing signal was taken from Clowe et al. (2004, 2006)). Using deep, high-resolution optical data from 3 ACS bands (F435W, F606W, and F814W), BVR data from Magellan and I-band from VLT/FORS (Clowe et al. 2004) they confirmed (based on photometry and morphology) six multiply imaged systems as discovered by Mehlert et al. (2001) (labeled A–F) and also identified 4 new additional systems (G–J) in the sub-cluster region, where none were previously known. The combined mass reconstruction of Bradač et al. (2006) provided a high-resolution, absolutely calibrated mass map, with a projected, enclosed mass  $M_{<250\text{kpc}} = 2.8 \pm 0.2 \times 10^{14} M_\odot$  around the main cluster and  $M_{<250\text{kpc}} = 2.3 \pm 0.2 \times 10^{14} M_\odot$  around the sub-cluster.

### 3.2 Critical evaluation of previously identified systems and new identification

We have reviewed each strongly lensed candidate proposed by Mehlert et al. (2001); Bradač et al. (2006, 2009) by checking the morphology and colour agreement as well as the consistency with the lensing mass model prediction. In the end, we have only used those systems that have been successfully verified. In order to avoid confusion between our and previous multiple image identification, we choose to redefine the notation of the multiple image systems going from 1 to 10 in the main cluster, and s1 to s6 in the sub-cluster.

Altogether, our set of constraints is quite different from the one of Bradač et al. (2009). Indeed, we have rejected 4



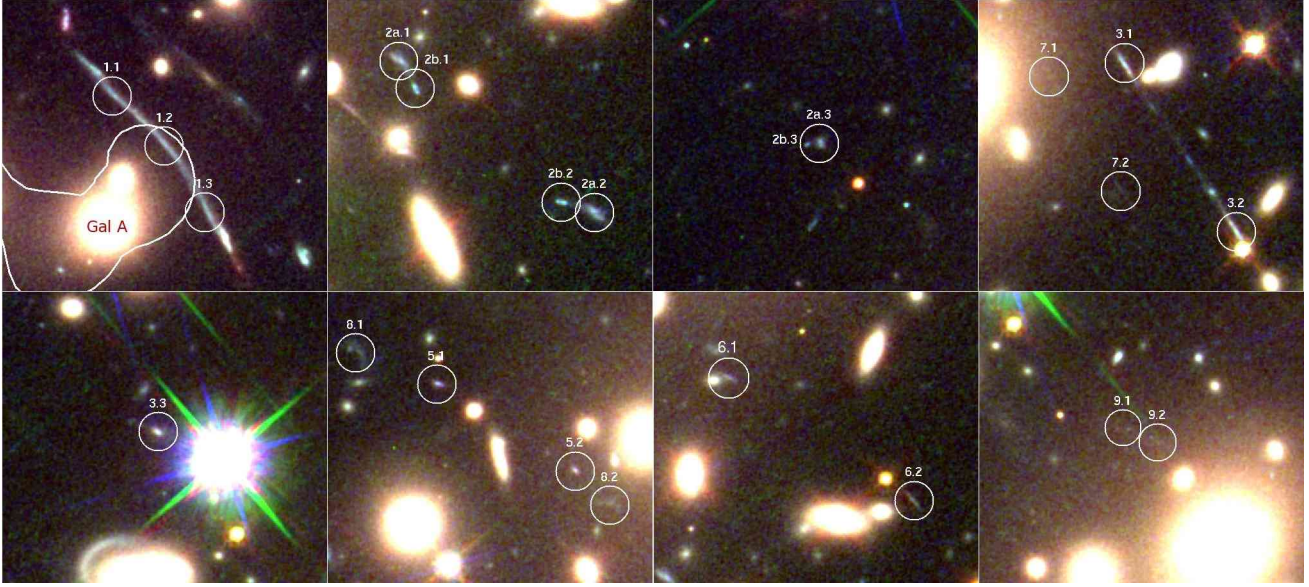


**Figure 4.** The multiple images identified in the main cluster area with the HST images, as shown in Figure 1. System 4 is not shown since it is invisible in ACS/HST. The size of each box is  $12'' \times 12''$ , North is up and East is left.

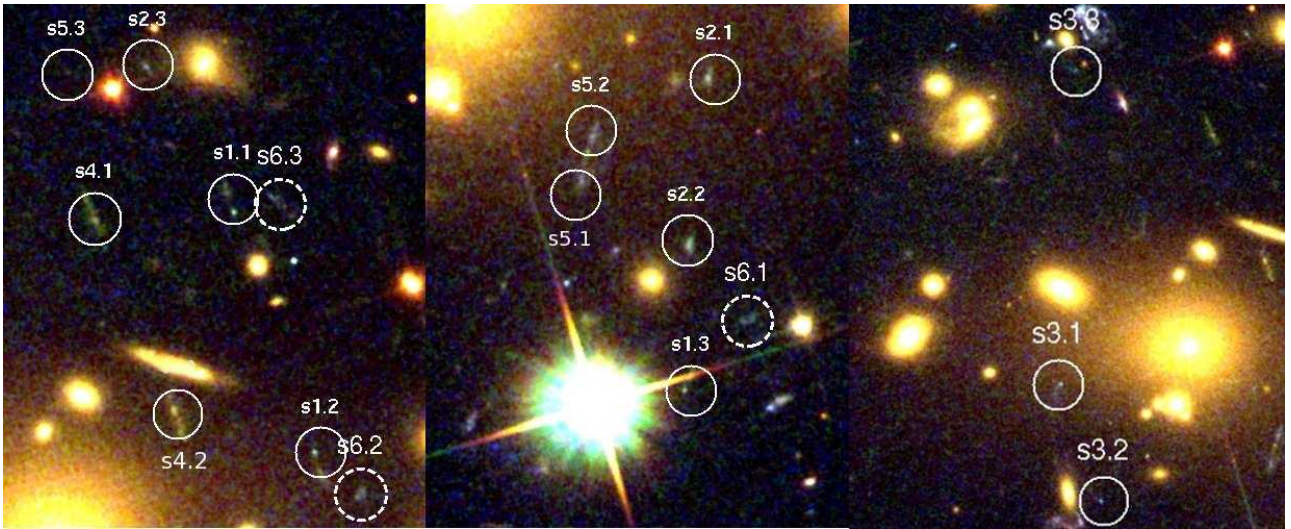


**Figure 5.** The multiple images identified in the sub cluster area with the ACS images, as shown in Figure 2. The size of each box is  $20'' \times 12''$ , North is up and East is left.

multiple-image systems (B, C, D and L) and changed system A and E, for the following reasons:

- system A: Bradač et al. (2006) matched two symmetric images A1 and A2 forming a giant arc, whereas the expected third image A3 is not detected. The analysis of Spitzer/MIPS and Herschel data of the Bullet Cluster performed by Rex et al. (2010) shows that only A1 is detected in the Far-IR (source HLS12 from this paper) and therefore the identification of the system is incorrect. To reconcile the identification with the far-infrared observations, we interpret the giant arc as the merging of 3 images crossing the critical line at  $z=3.24$  (system 1 in our notation) (see Figure 4);
- system B: according to our model (which now takes into account triply imaged system A) B is a single imaged arc;

- system C: the predicted third image is not detected, and the colors of the two images are in disagreement (the Northern C image is detected with Spitzer/MIPS, however the Southern is not, Pérez-González et al. 2010);

- system D: is problematic due to extended morphology and the large uncertainty in locating the different multiple image centers, thus we do not add it to the set of the systems that constrain the mass model, instead we use the mass model to predict images position and redshift (system 10 in our notation) (see Table 2);

- system E: (in our notation system 3), we find its third counter image 3.3;

- system L: the two images L1 and L2 have very different colors (L1 is brighter than L2 by  $\sim 0.5$  mag in all the filters except for F606W filter where L2 is detected with  $> 5 \sigma$  and

Name	F606	F435-F606	F606-F814
s2.1/I1	$26.26 \pm 0.04$	$0.50 \pm 0.13$	$0.08 \pm 0.08$
s2.2/I2	$26.03 \pm 0.04$	$0.48 \pm 0.12$	$0.04 \pm 0.08$
-/I3	$26.73 \pm 0.07$	$0.18 \pm 0.18$	$-0.22 \pm 0.15$
s2.3	$26.81 \pm 0.07$	$0.46 \pm 0.23$	$0.18 \pm 0.13$

**Table 1.** Photometry of the components of the multiply imaged system 's2' (corresponding to 'I' system in Bradač et al. 2006).

L1 is not detected with  $< 1.5 \sigma$ ), additionally, positions of multiple images is entirely excluded by the geometry of our model ( $\text{rms} > 10''$ ).

In the sub-cluster, we have also excluded/added the following images of the I, J and G systems:

- image I3 has a different colour than images I1 and I2 (s2.1 and s2.2 in our notation), instead we have found an object (s2.3) that better fits the position and colour of the system (see Table 1 and Figure 2);
- according to the geometry of our mass model, image G3 can not belong to the same system as images G1 and G2 (s4.1 and s4.2 in our notation). The model predicts position of the third counterpart (s4.3) of the system directly on the bright star, south of the cluster;
- we believe that G3 is a "straight" arc made of 2 merging images (named 's5.1' and 's5.2' in our notation, see Figure 2) with an identified third counterpart in the North part of the sub-cluster (s5.3);
- we find third image of the system J (s3.3 in our notation).

The three remaining multiply imaged systems from Bradač et al. (2009) F and K in the main cluster and H in the sub-cluster, were included in our set of constraints without changes.

Finally, we have identified 6 new multiple imaged systems, (5-9) in the main cluster thanks to the new deep WFC3 and ACS images and one new system s5 in the sub-cluster. We have also identified system s6 in the sub-cluster, however due to large uncertainties in the colour of this system we do not use it as a part of our model constraints but present it only as a possible multiple imaged candidate.

In Figure 4 and 5 we show postage stamps of all multiple images (except for system 4 that is not visible in HST/ACS and barely detected in HST/WFC3), their exact locations and redshifts are given in Table 2.

In total, we use 14 strongly lensed systems in this analysis (9 systems in the main cluster region and 5 systems in the sub-cluster region), three of those systems have measured spectroscopic redshifts. System 1 is the bright giant arc with previously measured redshift at  $z=3.24$  by Mehlert et al. (2001), we interpret it as a triple image in its center with the extremities of the arcs being taken as single images (See Figure 4). We have also two systems with newly measured spectroscopic redshift, system 4 which is an IRAC bright submm source, dusty galaxy (barely detected in the HST/WFC3 images, Gonzalez et al. 2010), with well measured redshift  $z=2.79$ , and system s1 at  $z=2.99$  measured with FORS/VLT (see Section 2.3).

## 4 LENSING METHODOLOGY

The strong-lensing mass reconstruction is based on the parametric, Bayesian Monte Carlo Markov chain (MCMC) method implemented in the LENSTOOL<sup>1</sup> software (Kneib et al. 1996; Jullo et al. 2007; Jullo & Kneib 2009).

The mass distribution of the Bullet Cluster is considered here as a superposition of three cluster-scale dark matter clumps (two in the main cluster and one in the sub-cluster), the BCGs, the intracluster gas and the individual galaxies.

The light distribution of the main cluster indicates cluster-scale dark matter bimodality. Nonetheless, we have checked the alternative possibility of main cluster consisting of only one dark matter clump. This alternative can not reproduce the position of the multiple images with as high accuracy as the two-clump model. It gives a significantly worse fit to the data ( $\text{rms} = 1.5''$  vs  $\text{rms} = 0.2''$ ), confirming the existence for two large scale dark matter halos in the main clump. Therefore, the dark matter clumps we call DM1 and DM2 in the bimodal main clump and DM3 for sub-clump.

All dark matter clumps and galaxies were parameterized as dual Pseudo Isothermal Elliptical mass distributions dPIE (Limousin et al. 2005). The dPIE is described by seven parameters: redshift, central position  $(x_c, y_c)$ , ellipticity  $\epsilon = \frac{a^2 - b^2}{a^2 + b^2}$ , (with  $a$  and  $b$  being semi-major and semi-minor axis, respectively), the position angle  $\theta$ , a core radius  $r_{\text{core}}$ , a truncated radius  $r_{\text{cut}}$  and a fiducial velocity dispersion  $\sigma$ . The two scale radii,  $r_{\text{core}}$  and  $r_{\text{cut}}$ , define changes in the slope of the dPIE density profile:

$$\rho(r) = \frac{\rho_0}{(1 + r^2/r_{\text{core}}^2)(1 + r^2/r_{\text{cut}}^2)}, \quad (1)$$

where  $\rho_0$  is a central density. The profile is flat in the inner region, then isothermal ( $\rho \sim r^{-2}$ ) between  $r_{\text{core}}$  and  $r_{\text{cut}}$ , and steeply decreasing ( $\rho \sim r^{-4}$ ) beyond  $r_{\text{cut}}$ . Thanks to its extra degree of freedom compared to a NFW potential, the dPIE potential is more flexible in modeling complex galaxy clusters, such as 1E 0657-56. Moreover, the dPIE profile is specially suitable to model galaxies. Indeed, several studies, based on dynamics of stars, globular clusters and X-ray halos have shown that early-type galaxies are isothermal in their inner parts (Koopmans et al. 2006; Oguri 2007; Gerhard et al. 2001; Peng et al. 2004), with no significant evolution with redshift up to  $z \sim 1$ , this is also true for cluster members (see Natarajan et al. 1998, 2004, 2009). The dPIE has been successfully used to model galaxy clusters (e.g. Kneib et al. 1996; Richard et al. 2007), as well as early-type galaxies (e.g. Natarajan et al. 1998; Limousin et al. 2007a).

In the optimization procedure the dPIE parameters of cluster scale DM halos were allowed to vary freely, the central position, ellipticity, velocity dispersion, core radius and the position angle. In case of the cluster galaxies, the position, ellipticity, and orientation were matched to that of the light distribution as measured by SExtractor. The velocity dispersions, core and cut-off radii of cluster members were scaled with their luminosity using common scaling relations (see Section 4.1).

<sup>1</sup> See <http://www.oamp.fr/cosmology/lenstool/>.

System	R.A. (deg)	Dec (deg)	F606W	606-775	775-850	850-110	110-160	$\mu$	$z_{\text{phot}}$	$z_{\text{m}}^a$	$z_{\text{spec}}$
1.1(A)	104.63293	-55.941725	25.59 $\pm$ 0.07	0.64 $\pm$ 0.09	0.02 $\pm$ 0.09	0.13 $\pm$ 0.08	0.41 $\pm$ 0.05	29.56 $\pm$ 8.97	3.98 <sup>+0.04</sup> <sub>-0.07</sub>	–	3.24
1.2	104.63158	-55.942454	25.65 $\pm$ 0.05	0.51 $\pm$ 0.09	0.09 $\pm$ 0.09	0.21 $\pm$ 0.07	0.42 $\pm$ 0.04	26.22 $\pm$ 6.68	3.09 <sup>+0.45</sup> <sub>-0.62</sub>	–	–
1.3(A)	104.63055	-55.943405	25.67 $\pm$ 0.06	0.66 $\pm$ 0.11	0.02 $\pm$ 0.09	0.02 $\pm$ 0.08	0.37 $\pm$ 0.06	12.48 $\pm$ 0.90	3.17 <sup>+0.03</sup> <sub>-0.14</sub>	–	–
2a.1(F) <sup>b</sup>	104.65210	-55.956245	24.63 $\pm$ 0.06	0.30 $\pm$ 0.08	-0.07 $\pm$ 0.09	0.15 $\pm$ 0.08	0.42 $\pm$ 0.05	9.77 $\pm$ 0.44	2.86 <sup>+0.35</sup> <sub>-0.25</sub>	2.14 $\pm$ 0.19	–
2a.2(F)	104.64704	-55.958497	24.12 $\pm$ 0.05	0.22 $\pm$ 0.03	-0.08 $\pm$ 0.03	0.18 $\pm$ 0.03	0.41 $\pm$ 0.05	11.11 $\pm$ 0.72	2.70 <sup>+0.61</sup> <sub>-0.24</sub>	–	–
2a.3(F)	104.66515	-55.951289	25.33 $\pm$ 0.11	0.37 $\pm$ 0.15	-0.01 $\pm$ 0.15	0.08 $\pm$ 0.14	0.52 $\pm$ 0.09	4.89 $\pm$ 0.22	2.96 <sup>+0.20</sup> <sub>-0.14</sub>	–	–
2b.1 <sup>b</sup>	104.65165	-55.956641	25.31 $\pm$ 0.09	0.30 $\pm$ 0.08	-0.07 $\pm$ 0.09	0.14 $\pm$ 0.08	0.39 $\pm$ 0.08	14.91 $\pm$ 1.11	3.10 <sup>+0.54</sup> <sub>-0.93</sub>	–	–
2b.2	104.64786	-55.958292	25.09 $\pm$ 0.12	0.24 $\pm$ 0.04	-0.03 $\pm$ 0.04	0.06 $\pm$ 0.04	0.13 $\pm$ 0.10	15.02 $\pm$ 0.96	2.85 <sup>+0.35</sup> <sub>-0.40</sub>	–	–
2b.3	104.66544	-55.951301	26.61 $\pm$ 0.36	0.45 $\pm$ 0.11	-0.08 $\pm$ 0.11	0.04 $\pm$ 0.10	0.27 $\pm$ 0.09	4.77 $\pm$ 0.21	3.98 <sup>+1.62</sup> <sub>-0.19</sub>	–	–
3.1(E)	104.64242	-55.948720	25.52 $\pm$ 0.05	0.49 $\pm$ 0.08	0.11 $\pm$ 0.07	0.15 $\pm$ 0.06	0.43 $\pm$ 0.08	15.96 $\pm$ 1.36	3.50 <sup>+0.38</sup> <sub>-0.45</sub>	3.17 $\pm$ 0.27	–
3.2(E)	104.63954	-55.951165	25.51 $\pm$ 0.04	0.55 $\pm$ 0.08	0.22 $\pm$ 0.06	0.11 $\pm$ 0.05	0.37 $\pm$ 0.05	16.72 $\pm$ 1.30	3.16 <sup>+0.39</sup> <sub>-0.50</sub>	–	–
3.3	104.65434	-55.944392	25.77 $\pm$ 0.04	0.45 $\pm$ 0.07	0.33 $\pm$ 0.06	0.20 $\pm$ 0.05	0.42 $\pm$ 0.06	7.13 $\pm$ 0.40	2.96 <sup>+0.01</sup> <sub>-0.02</sub>	–	–
4(K)	104.65864	-55.950557	–	–	–	–	–	–	–	–	2.79
4(K)	104.65459	-55.951876	–	–	–	–	–	–	–	–	–
4(K)	104.63929	-55.958032	–	–	–	–	–	–	–	–	–
5.1	104.65560	-55.948760	25.62 $\pm$ 0.06	0.32 $\pm$ 0.21	0.27 $\pm$ 0.26	0.21 $\pm$ 0.21	0.51 $\pm$ 0.11	10.61 $\pm$ 0.40	2.96 <sup>+0.02</sup> <sub>-0.02</sub>	2.91 $\pm$ 0.25	–
5.2	104.65203	-55.950014	24.59 $\pm$ 0.06	0.56 $\pm$ 0.12	0.24 $\pm$ 0.09	0.21 $\pm$ 0.08	0.49 $\pm$ 0.05	14.18 $\pm$ 0.94	3.09 <sup>+0.73</sup> <sub>-0.29</sub>	–	–
5.3	104.63801	-55.956311	26.35 $\pm$ 0.07	0.45 $\pm$ 0.16	0.44 $\pm$ 0.13	0.25 $\pm$ 0.10	0.57 $\pm$ 0.08	4.79 $\pm$ 0.21	2.74 <sup>+0.10</sup> <sub>-0.02</sub>	–	–
6.1	104.65049	-55.953339	27.20 $\pm$ 0.13	0.25 $\pm$ 0.17	0.19 $\pm$ 0.25	0.89 $\pm$ 0.18	0.17 $\pm$ 0.04	15.65 $\pm$ 1.20	2.03 <sup>+0.96</sup> <sub>-0.54</sub>	1.21 $\pm$ 0.23	–
6.2	104.64572	-55.955109	26.83 $\pm$ 0.11	0.29 $\pm$ 0.09	0.30 $\pm$ 0.07	0.50 $\pm$ 0.05	0.24 $\pm$ 0.05	11.20 $\pm$ 0.57	1.39 <sup>+1.07</sup> <sub>-0.39</sub>	–	–
6.3	104.65706	-55.950866	–	–	–	–	–	–	–	–	–
7.1	104.64423	-55.949050	27.58 $\pm$ 0.38	0.21 $\pm$ 0.12	0.57 $\pm$ 0.04	-0.29 $\pm$ 0.04	-0.08 $\pm$ 0.05	22.96 $\pm$ 2.11	2.03 <sup>+1.1</sup> <sub>-0.42</sub>	2.00 $\pm$ 0.12	–
7.2	104.64251	-55.950576	26.97 $\pm$ 0.28	0.28 $\pm$ 0.14	0.36 $\pm$ 0.07	-0.33 $\pm$ 0.05	-0.20 $\pm$ 0.04	20.04 $\pm$ 1.71	0.17 <sup>+2.28</sup> <sub>-0.12</sub>	–	–
7.3	104.65166	-55.944823	–	–	–	–	–	–	–	–	–
8.1	104.65770	-55.948271	24.74 $\pm$ 0.05	0.61 $\pm$ 0.18	-0.01 $\pm$ 0.07	-0.09 $\pm$ 0.05	0.23 $\pm$ 0.02	9.37 $\pm$ 0.54	4.16 <sup>+0.22</sup> <sub>-0.25</sub>	4.06 $\pm$ 1.23	–
8.2	104.65118	-55.950472	26.74 $\pm$ 0.08	0.95 $\pm$ 0.32	-0.22 $\pm$ 0.17	-0.26 $\pm$ 0.15	0.38 $\pm$ 0.12	4.73 $\pm$ 0.14	4.32 <sup>+0.28</sup> <sub>-0.14</sub>	–	–
8.3	104.63565	-55.957061	> 28.50	> 1.51	-0.34 $\pm$ 0.07	-0.05 $\pm$ 0.27	0.53 $\pm$ 0.24	4.94 $\pm$ 0.22	4.53 <sup>+0.42</sup> <sub>-0.55</sub>	–	–
9.1	104.64961	-55.947382	27.44 $\pm$ 0.23	1.14 $\pm$ 0.21	-0.72 $\pm$ 0.19	-0.06 $\pm$ 0.17	0.26 $\pm$ 0.35	4.70 $\pm$ 0.20	2.10 <sup>+0.38</sup> <sub>-0.21</sub>	2.54 $\pm$ 0.34	–
9.2	104.64928	-55.947412	27.56 $\pm$ 0.45	0.90 $\pm$ 0.18	-0.31 $\pm$ 0.12	-0.40 $\pm$ 0.10	0.21 $\pm$ 0.26	4.75 $\pm$ 0.20	2.00 <sup>+0.53</sup> <sub>-0.18</sub>	–	–
9.3	104.63731	-55.953223	–	–	–	–	–	–	–	–	–
10.1 <sup>c</sup>	104.63940	-55.947582	26.79 $\pm$ 0.24	-0.49 $\pm$ 0.35	0.49 $\pm$ 0.33	0.13 $\pm$ 0.22	0.30 $\pm$ 0.17	50.19 $\pm$ 5.42	2.56 <sup>+0.74</sup> <sub>-0.38</sub>	3.23 $\pm$ 0.42	–
10.2	104.63843	-55.948325	26.74 $\pm$ 0.20	-0.13 $\pm$ 0.10	0.99 $\pm$ 0.14	-0.03 $\pm$ 0.52	0.37 $\pm$ 0.11	49.83 $\pm$ 10.34	2.34 <sup>+0.24</sup> <sub>-0.45</sub>	–	–
10.3(D)	104.64806	-55.943810	26.59 $\pm$ 0.22	0.45 $\pm$ 0.25	0.04 $\pm$ 0.22	0.30 $\pm$ 0.12	0.20 $\pm$ 0.31	9.96 $\pm$ 3.23	2.13 <sup>+0.85</sup> <sub>-0.89</sub>	–	–

**Table 2.** The multiply imaged systems used to constrain the model, with their centroid position, brightness, colors, linear magnification and predicted or spectroscopically measured redshifts. The systems and their properties, along with references to the papers reporting their redshifts, are given in Section 3. <sup>a</sup> Redshift estimation inferred from the mass model when all spectroscopically confirmed multiply imaged systems have been included in the optimization. <sup>b</sup> System 2a and 2b are most probably gravitationally bounded. <sup>c</sup> System 10 is not included in the model optimization, it is a multiple imaged candidate. Numbers (.1, .2, etc) denote the different images of each set of multiple images, each presented in Figure 4, except system 4 that is invisible in optical and system 10 that has not been included in the model optimization.

BCGs and the 2 cluster galaxies that are in the vicinity of multiple images were fitted individually, the same approach was used in lens modeling by Suyu & Halkola (2010); Limousin et al. (2008, 2007b); Richard et al. (2010b,a). Firstly, because both BCG and galaxies that are in the vicinity of multiple images have strong influence on the multiple images position. Secondly, because BCGs are likely distinct galaxy population from cluster ellipticals, hence they do not follow common scaling laws (Natarajan et al. 1998). The two galaxies that are used explicitly in the optimization procedure are: galaxy A (104.63308, -55.943594) which strongly affects the brightest tangential arc (system 1) and galaxy B (104.65626, -55.950795) which affects the multiple imaged systems 2, 4 and 5 (see Figure 1 and 6).

The baryonic matter content of galaxy clusters is dominated by the X-ray emitting intracluster gas, the mass of which reaches 10-15% (David et al. 1993; Neumann & Arnaud 2001; Vikhlinin et al. 2006; LaRoque et al. 2006) of the total mass. As the emissivity of the X-ray emitting gas is proportional to the square of its density, the gas mass profile in a cluster can be precisely determined from X-ray

data. In the case of the Bullet Cluster there is a significant offset between the gas and dark matter distribution. Because of this offset, including the gas mass as a separate component is important for accurate modeling of the total mass distribution. Therefore, we have included the intracluster gas (without optimization of this component) in our total mass model of the Bullet Cluster (see Section 4.3) using the X-rays measurements performed by Ota & Mitsuda (2004); Markevitch et al. (2002).

Using the observational constraints (multiply imaged systems) we have optimized the parameters of the mass components: the DM clumps, the BCGs and the individual galaxies (see Table 4). As a starting point, we have used a set of initial parameters (centroid, ellipticity and position angle) based on the visible component, Limousin et al. (2008) that were then iteratively optimized.

For each image we find its rms (root-mean-square) value for its position in the image plane, given by  $\text{rms} = \sqrt{\frac{1}{n} \sum_{j=1}^n (X_{\text{obs}}^j - X)^2}$ , where  $n$  is the number of images for the system,  $X$  is the position in the image plane and  $X_{\text{obs}}$

System	RA. (deg)	Dec (deg)	F606W	F435W-F606W	F606W-F814W	F435W-F814W	$\mu$	$z_{\text{phot}}$	$z_{\text{m}}^a$	$z_{\text{spec}}$
Sub Clump										
s1.1(H)	104.56305	-55.939755	$26.59 \pm 0.08$	$0.65 \pm 0.11$	$-0.21 \pm 0.07$	$0.43 \pm 0.12$	$6.48 \pm 0.67$	$3.3^{+0.2}_{-1.2}$	—	2.99
s1.2(H)	104.56145	-55.942423	$26.78 \pm 0.08$	$0.78 \pm 0.14$	$-0.40 \pm 0.09$	$0.36 \pm 0.16$	$9.62 \pm 0.87$	$3.3^{+0.2}_{-0.7}$	—	—
s1.3(H)	104.56202	-55.947717	$26.57 \pm 0.12$	$1.00 \pm 0.15$	$-0.29 \pm 0.06$	$0.29 \pm 0.14$	$11.74 \pm 1.53$	$2.7^{+0.9}_{-1.3}$	—	—
s2.1	104.56155	-55.944252	$25.55 \pm 0.07$	$0.50 \pm 0.07$	$0.08 \pm 0.04$	$0.59 \pm 0.07$	$20.25 \pm 3.38$	$2.6^{+0.7}_{-1.3}$	$3.24 \pm 0.13$	—
s2.2(I)	104.56192	-55.946101	$25.60 \pm 0.05$	$0.49 \pm 0.06$	$0.03 \pm 0.04$	$0.52 \pm 0.06$	$15.91 \pm 1.53$	$2.6^{+0.7}_{-1.5}$	—	—
s2.3(I)	104.56478	-55.938146	$26.36 \pm 0.14$	$0.47 \pm 0.11$	$0.17 \pm 0.07$	$0.64 \pm 0.11$	$5.31 \pm 0.50$	$2.4^{+0.9}_{-1.4}$	—	—
s3.1(J)	104.57038	-55.944036	$26.81 \pm 0.13$	$-0.11 \pm 0.08$	$-0.47 \pm 0.09$	$-0.58 \pm 0.10$	$24.49 \pm 4.01$	$1.6^{+1.2}_{-0.6}$	$2.02 \pm 0.25$	—
s3.2(J)	104.56917	-55.946003	$27.03 \pm 0.12$	$-0.32 \pm 0.10$	$-0.19 \pm 0.10$	$-0.50 \pm 0.11$	$19.33 \pm 1.99$	$1.0^{+1.8}_{-0.0}$	—	—
s3.3	104.56993	-55.938772	$27.99 \pm 0.55$	$-0.17 \pm 0.21$	$-0.37 \pm 0.16$	$-0.20 \pm 0.18$	$5.39 \pm 0.48$	$0.9^{+2.3}_{-0.9}$	—	—
s4.1(G)	104.56580	-55.939857	$25.31 \pm 0.05$	$> 1.85$	$0.40 \pm 0.05$	$> 2.25$	$11.60 \pm 1.56$	$3.3^{+1.5}_{-2.3}$	$0.73 \pm 0.09$	—
s4.2(G)	104.56424	-55.941963	$25.27 \pm 0.06$	$> 1.73$	$0.57 \pm 0.06$	$> 2.16$	$13.46 \pm 1.04$	$2.5^{+1.3}_{-0.8}$	—	—
s4.3	104.56471	-55.947724	—	—	—	—	—	—	—	—
s5.1(G)	104.56406	-55.945386	$26.05 \pm 0.08$	$-0.14 \pm 0.09$	$0.25 \pm 0.07$	$0.11 \pm 0.08$	$40.90 \pm 4.88$	$0.9^{+1.1}_{-0.6}$	$2.51 \pm 0.12$	—
s5.2	104.56384	-55.944904	$26.17 \pm 0.11$	$-0.08 \pm 0.09$	$0.15 \pm 0.08$	$0.07 \pm 0.09$	$31.30 \pm 5.68$	$0.8^{+1.9}_{-0.8}$	—	—
s5.3	104.56627	-55.938208	$> 28.45$	—	—	—	$4.86 \pm 0.43$	—	—	—
s6.1 <sup>b</sup>	104.56084	-55.946952	$26.89 \pm 0.15$	$0.07 \pm 0.35$	$-0.36 \pm 0.45$	$-0.29 \pm 0.23$	$22.71 \pm 3.39$	$1.4^{+1.9}_{-0.5}$	$3.00 \pm 0.19$	—
s6.2	104.56054	-55.942898	$26.54 \pm 0.12$	$0.15 \pm 0.22$	$0.03 \pm 0.32$	$0.18 \pm 0.13$	$16.79 \pm 1.90$	$2.2^{+1.5}_{-1.5}$	—	—
s6.3	104.56230	-55.939588	$26.89 \pm 0.13$	$0.03 \pm 0.34$	$0.25 \pm 0.29$	$0.28 \pm 0.38$	$10.94 \pm 0.78$	$0.5^{+3.0}_{-0.4}$	—	—

**Table 3.** The multiply imaged systems used to constrain the model, with their centroid position, brightness, colors, linear magnification and predicted or spectroscopically measured redshifts. The systems and their properties, along with references to the papers reporting their redshifts, are given in Section 3. <sup>a</sup> Redshift estimation inferred from the mass model when all spectroscopically confirmed multiply imaged systems have been included in the optimization. <sup>b</sup> System s6 is not included in the model optimization, it is multiple imaged candidate. Numbers (.1, .2, etc) denote the different images of each set of multiple images, each presented in Figure 5, except system s6 that has not been included in the model optimization.

the observed position in the image plane. The overall rms is defined by summing and averaging over all the images for all the systems. A detailed overview of the LENSTOOL software can be found in Jullo et al. (2007).

Thanks to the new parallelized version of LENSTOOL the optimization could be efficiently performed in the image plane similarly as done in Limousin et al. (2011).

#### 4.1 Scaling relation of elliptical cluster members

We lack sufficient sensitivity to constrain the detailed mass profile for individual cluster galaxies. Thus, in general, parametric cluster modeling uses Faber-Jackson scaling relation (FJR) (Faber & Jackson 1976) to scale the galaxy members. It assumes that all galaxies in the cluster have the same M/L ratio (Natarajan & Kneib 1997; Natarajan et al. 1998; Limousin et al. 2007b; Oguri 2010; Limousin et al. 2005; Kneib et al. 2003; Richard et al. 2009; Jullo et al. 2010).

However, FJR is just an empirical relation with a large scatter. For example, Nigoche-Netro et al. (2010) by analyzing the FJR showed that its parameters depend on the magnitude range.

In fact FJR is a projection of the Fundamental Plane (FP) relation. The Fundamental Plane (Djorgovski & Davis 1987) is a tight correlation for elliptical galaxies between  $R_e$  the effective radius,  $\sigma$  the central velocity dispersion, and  $\langle I \rangle_e$  the mean effective surface brightness, and can read:

$$\log R_e = a \log \sigma_{\text{FP}} + b \log \langle I \rangle_e + c, \quad (2)$$

where  $a$ ,  $b$ ,  $c$  are free parameters of this relation.

It is understood that the FP is a consequence of the dynamical equilibrium condition of elliptical galaxies. FP has

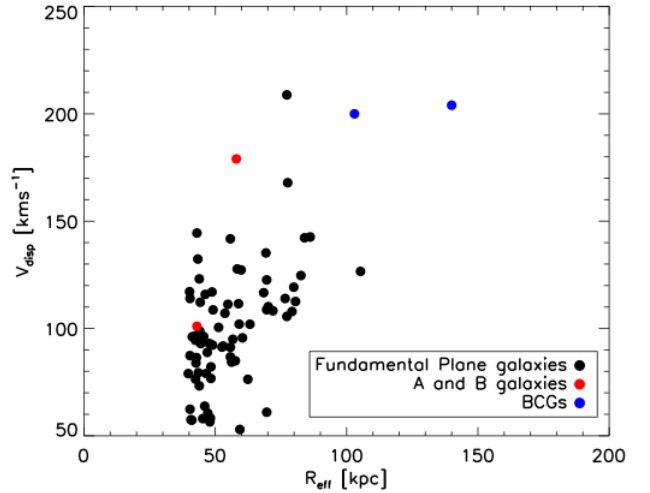


**Figure 6.** The galaxy members identified using color-color cut and comparison of the properties with separately modeled galaxies A and B (red) and BCGs (blue).

been successfully used in various studies describing elliptical galaxies and in strong lens mass modeling by e.g. D'Aloisio & Natarajan (2011); Jullo et al. (2007); Halkola et al. (2006); Natarajan & Kneib (1997). Therefore in this paper we have applied FP to scale early-type cluster members.

For FP we use parameters derived by Bernardi et al. (2003),  $a = 1.49$ ,  $b = -0.74$ ,  $c = 8.779$ , which galaxy sample has similar properties to the galaxy members in the Bullet Cluster.

Bernardi et al. (2003) have used a magnitude-limited



System	$\Delta\alpha$ ( $''$ )	$\Delta\delta$ ( $''$ )	$\epsilon$	$\theta^a$	$r_{core}$ (kpc)	$r_{cut}$ (kpc)	$\sigma_0$ ( $\text{kms}^{-1}$ )
FJ log(Evidence)=-35.1							
DM 1	$4.94 \pm 0.19$	$0.84 \pm 2.52$	$0.49 \pm 0.01$	$79.8 \pm 1.5$	$133.43 \pm 5.9$	[1000.0]	$857.66 \pm 61.52$
DM 2	$29.63 \pm 0.33$	$25.02 \pm 0.80$	$0.59 \pm 0.01$	$60.8 \pm 1.1$	$163.67 \pm 17.1$	[1000.0]	$896.14 \pm 29.87$
DM 3	$189.78 \pm 0.44$	$49.28 \pm 0.18$	$0.11 \pm 0.02$	$29.8 \pm 2.3$	$72.5 \pm 0.9$	[1000.0]	$960.39 \pm 21.93$
BCG 1	[0.00]	[0.00]	[0.26]	[43.5]	[0.3]	$150.0 \pm 2.1$	$255.85 \pm 39.34$
BCG 2	[24.05]	[29.13]	[0.20]	[37.4]	[0.2]	$112.2 \pm 1.8$	$201.60 \pm 2.38$
Gal A	[51.94]	[48.93]	[0.13]	[9.9]	[0.1]	$60.0 \pm 0.9$	$199.33 \pm 3.88$
Gal B	[5.23]	[23.01]	[0.10]	[-49.0]	[0.1]	$53.3 \pm 1.3$	$105.07 \pm 1.64$
$\sigma_{FJ}^*$	...	...	...	...	[0.1]	$48.63 \pm 8.53$	$119.20 \pm 5.05$
FP+TF log(Evidence)=-36.8							
DM 1	$4.93 \pm 0.32$	$-4.97 \pm 0.69$	$0.50 \pm 0.02$	$79.8 \pm 0.8$	$121.23 \pm 4.9$	[1000.0]	$897.91 \pm 85.11$
DM 2	$29.98 \pm 0.20$	$30.03 \pm 0.89$	$0.59 \pm 0.01$	$56.5 \pm 1.8$	$155.1 \pm 9.1$	[1000.0]	$861.30 \pm 30.69$
DM 3	$189.17 \pm 0.23$	$49.59 \pm 0.17$	$0.17 \pm 0.02$	$18.5 \pm 1.9$	$59.6 \pm 0.9$	[1000.0]	$847.65 \pm 22.21$
BCG 1	[0.00]	[0.00]	[0.26]	[43.5]	[0.3]	$140.2 \pm 12.3$	$203.80 \pm 39.34$
BCG 2	[24.05]	[29.13]	[0.20]	[37.4]	[0.2]	$102.6 \pm 5.8$	$200.35 \pm 6.94$
Gal A	[51.94]	[48.93]	[0.13]	[9.9]	[0.1]	$58.1 \pm 10.1$	$179.55 \pm 9.11$
Gal B	[5.23]	[23.01]	[0.10]	[-49.0]	[0.1]	$42.9 \pm 2.2$	$101.23 \pm 5.07$
FP	...	...	...	...	[0.1]	$71.81 \pm 5.07$	$0.93 \pm 0.04^b$
$\sigma_{TF}^*$	...	...	...	...	[0.1]	$41.09 \pm 1.25$	$107.14 \pm 7.08$
Xray+FP+TF log(Evidence)=-33.8							
DM 1	$4.97 \pm 0.16$	$1.95 \pm 1.29$	$0.56 \pm 0.02$	$85.2 \pm 2.1$	$105.9 \pm 4.9$	[1000.0]	$814.04 \pm 57.24$
DM 2	$29.92 \pm 0.10$	$25.12 \pm 0.88$	$0.57 \pm 0.01$	$54.3 \pm 1.6$	$117.9 \pm 9.1$	[1000.0]	$717.35 \pm 22.69$
DM 3	$189.78 \pm 0.26$	$49.28 \pm 0.53$	$0.15 \pm 0.02$	$15.8 \pm 2.2$	$52.2 \pm 0.9$	[1000.0]	$788.25 \pm 23.28$
BCG 1	[0.00]	[0.00]	[0.26]	[43.5]	[0.3]	$157.5 \pm 2.1$	$303.03 \pm 34.45$
BCG 2	[24.05]	[29.13]	[0.20]	[37.4]	[0.2]	$134.3 \pm 1.5$	$187.21 \pm 5.72$
Gal A	[51.94]	[48.93]	[0.13]	[9.9]	[0.1]	$66.3 \pm 1.1$	$170.95 \pm 8.23$
Gal B	[5.23]	[23.01]	[0.10]	[-49.0]	[0.1]	$45.5 \pm 1.5$	$108.73 \pm 5.76$
FP	...	...	...	...	[0.1]	$74.14 \pm 3.53$	$0.91 \pm 0.03^b$
$\sigma_{TF}^*$	...	...	...	...	[0.1]	$47.12 \pm 1.04$	$101.65 \pm 10.33$

**Table 4.** Modeled parameters of the three different mass model approaches. **Top** - model with Faber-Jackson scaling relation, **Middle** - model with Fundamental Plane and Tully-Fisher scaling relation and **Bottom** - our final model with explicitly included X-rays gas mass plus Fundamental Plane and Tully-Fisher scaling relations. Values quoted within brackets were kept fixed in the optimization. The error bars correspond to 68% confidence levels. The location and the ellipticity of the matter clumps associated with the cluster galaxies were kept fixed according to the light distribution. The ellipticity  $\epsilon$  is the one of the mass distribution, expressed as  $a^2 - b^2/a^2 + b^2$ . The center is defined at  $\alpha = 104.6588589$   $\delta = -55.9571863$  in J2000 coordinates corresponding to the center of the first BCG.

<sup>a</sup> Position angle of the potential distribution expressed in degree,  $90^\circ$  relative to PA. It corresponds to the direction of the semi-minor axis of the isopotential counted from the horizontal axis, counterclockwise.

<sup>b</sup> This is Fundamental Plane parameter described in Eq. 3, it is a factor S that translates  $\sigma_{FP}$  into  $\sigma_{dPIE}$

sample of nearly 9000 early-type galaxies in the redshift range  $0.01 < z < 0.3$  that was selected from the Sloan Digital Sky Survey (SDSS) using morphological and spectral criteria. They concluded that FP parameters depend very little on the sample redshifts at  $0.01 < z < 0.3$  and likewise they found only slight dependence on environment.

We have derived  $\sigma_{FP}$  for each cluster members (see Eq. 2) using the two observables  $\langle I \rangle_e$  and  $R_e$  obtained from SEXTRACTOR. We have then scaled the  $\sigma_{FP}$  by the factor  $S$  that is optimized in the modeling process, because  $\sigma_{FP}$  and  $\sigma_{dPIE}$  differ by the radius over which they are measured,  $r_{cut} \gg R_e$  (the galaxy mass component is including both stellar mass and dark matter mass). Summarizing we have:

$$\sigma_0 = S\sigma_{FP} \quad (3)$$

$$r_{cut} = r_{cut}^* \left( \frac{L}{L^*} \right)^{1/2}, \quad (4)$$

$$r_{core} = r_{core}^* \left( \frac{L}{L^*} \right)^{1/2}, \quad (5)$$

where  $L^*$ ,  $r_{core}^*$  and  $r_{cut}^*$  are, the luminosity, core radius and cut radius, the dPIE parameters of a typical cluster galaxy (Limousin et al. 2007b).

## 4.2 Scaling relation of the spiral cluster members

The cluster members of any cluster consist of both spiral and elliptical galaxies. In the previous parametric modeling of galaxy clusters (Limousin et al. 2007b, 2005; Kneib et al. 2003; Richard et al. 2009; Jullo et al. 2010), those two different galaxy types were scaled with a common scaling law. Here we divide the cluster members in two distinct groups. Using visual verification we have found 18 spiral galaxies within the 100 brightest cluster members. While, elliptical galaxies are scaled using FP as described in previous Section, spirals are scaled using the Tully-Fisher (TF) relation

System	(1) rms <sub>FJ</sub> (")	(2) rms <sub>FP+TF</sub> (")	(3) rms <sub>Xrays</sub> (")
1.1	0.145	0.231	0.128
1.2	0.026	0.026	0.068
1.3	0.119	0.131	0.061
2a.1	0.205	0.065	0.156
2a.2	0.274	0.247	0.110
2a.3	0.128	0.069	0.178
2b.1	0.183	0.363	0.154
2b.2	0.253	0.284	0.109
2b.3	0.102	0.179	0.160
3.1	0.247	0.305	0.329
3.2	0.254	0.193	0.077
3.3	0.290	0.182	0.257
4.1	0.300	0.088	0.393
4.2	0.132	0.018	0.228
4.3	0.215	0.162	0.201
5.1	0.150	0.126	0.197
5.2	0.085	0.031	0.184
5.3	0.164	0.067	0.063
6.1	0.252	0.269	0.182
6.2	0.551	0.953	0.182
7.1	0.172	0.152	0.113
7.2	0.075	0.237	0.113
8.1	0.046	0.081	0.258
8.2	0.046	0.070	0.258
8.3	0.046	0.070	0.258
9.1	0.096	1.11	0.076
9.2	0.056	0.870	0.076
s1.1	0.237	0.380	0.100
s1.2	0.209	0.243	0.119
s1.3	0.076	0.048	0.023
s2.1	0.367	0.479	0.105
s2.2	0.356	0.291	0.037
s2.3	0.082	0.118	0.075
s3.1	0.084	0.123	0.033
s3.2	0.084	0.190	0.033
s3.3	0.145	1.450	0.033
s4.1	0.345	0.983	0.126
s4.2	0.045	0.486	0.126
s5.1	0.054	0.123	0.080
s5.2	0.078	0.256	0.028
s5.3	0.752	1.647	0.053
Average	0.197	0.202	0.158

**Table 5.** Goodness of fit of the three different Bullet Cluster models: (1) Faber Jackson relation, (2) Fundamental Plane+Tully-Fisher, and (3) X-rays with Fundamental Plane+Tully-Fisher. The rms represent the difference between measured position of the images and the position predicted by the model.

(Tully & Fisher 1977). TF relation is an empirical relation between the intrinsic luminosity of a spiral galaxy and its velocity dispersion. Hence, central velocity dispersion is described as follows,

$$\sigma_0 = \sigma_0^* \left( \frac{L}{L^*} \right)^{1/4}, \quad (6)$$

where  $L^*$ ,  $\sigma_0^*$  are the dPIE parameters, the luminosity and central velocity dispersion, of a typical cluster galaxy (Limousin et al. 2007b). While the truncated radius  $r_{\text{cut}}$  and core radius  $r_{\text{core}}$ , are linked with luminosity by scaling relations described in Eq. 4 and 5, respectively.

We have optimized our model using both methods (1) the standard FJ – for all members and (2) using the FP for elliptical galaxies, and the Tully-Fisher relation for spirals; in order to see the impact of these different relations on the modeling accuracy. The comparison of the two scalings is described in the Section 4.4.

### 4.3 X-rays

Gas in galaxy clusters represent  $\sim 10\text{--}15\%$  of the total mass, which can be fairly easily measured with X-rays (e.g. David et al. 1993; Neumann & Arnaud 2001; Vikhlinin et al. 2006; LaRoque et al. 2006). However, gas is generally not included explicitly in cluster lens modeling (with some small exceptions, e.g. Bradač et al. 2008). This is partly due to the fact that in relaxed clusters gas traces dark matter hence it can not be disentangled from the dark matter component.

However, in the Bullet Cluster there is a significant offset between the gas and dark matter distribution. Thus, including the gas mass as a separate component of the mass model is essential for realistic modeling the total mass distribution of the bullet cluster. Moreover, due to the offset, gas distribution in this cluster has been well studied (Ota & Mitsuda 2004; Markevitch et al. 2002).

X-ray emission in the intracluster gas is dominated by thermal bremsstrahlung, and it is proportional to the line-of-sight integral of the square of the electron density. Due to lack of strongly lensed images in vicinity of the gas density centers we expect that the gas mass in the Bullet Cluster provides only an external shear to the strong lens model. However, to compare the effect of the gas mass distribution on the results, we create two fiducial models for the spatial distribution of the total (main+sub) intracluster gas mass.

For our fiducial model X1, we take the spatial distribution of the total (main+sub) intracluster gas as a spherical model derived from ROSAT HRI measurements resolution of Ota & Mitsuda (2004),  $\beta = 1.04$ ,  $\theta_c = 112.5''$ ,  $n_{e0} = 7.2 \times 10^{-3} \text{ cm}^{-3}$ . And we obtain a surface gas mass map by projection of the  $\beta$ -model gas density profile:

$$M_{\text{gas},2\text{D}}(r) = 2 \rho_{\text{gas},0} r_c g(\beta) \left( 1 + \frac{r^2}{r_c^2} \right)^{-3\beta/2+1/2} \quad (7)$$

with  $g(\beta) = 1/2 \Gamma(1/2) \Gamma(3\beta/2 - 1/2) / \Gamma(3\beta/2)$ ,  $\rho_{\text{gas},0}$  the gas mass density at the centre and  $r_c$  the core radius.

In the second fiducial model X2, we assume as an approximation that X-ray emission is proportional to the square of the mass density. We assume that this is tenable in the central region.

We take a square root of the smoothed (convolution by a Gaussian of  $\sigma = 2$  pixels) X-ray count map from the 500 ks Chandra ACIS-I observations (Markevitch 2006) and we normalize it. Since our purpose here is to create a very rough gas mass map in a small region, we are deliberately skipping the projection issue of the density map (Ettori 2000).

In order to find the normalization factor, due to the projection effect, we take the  $\beta$  model derived from above mentioned ROSAT HRI measurements of X-ray gas mass ( $\sim 2''$  resolution). The total mass within  $30''$  radius of this projected model,  $2.1 \times 10^{13} M_\odot$  was the normalization factor.

We have included the X-rays gas mass maps into our lens model using the grid technique implemented in

LENSTOOL (Jullo & Kneib 2009), and compared the results for the 2 different fiducial models. The code iteratively splits the  $200'' \times 200''$  mass map into equilateral triangles as a function of a mass threshold. At each node of this multi-scale grid a mass profile is described by a dPIE potential whose core radius is equal to the local grid resolution and a cut-off radius equals to three times the core radius. We force the algorithm to stop after four levels of splitting and as a result we have a grid cell containing  $\sim 50$  dPIE potentials describing the smooth gas distribution.

#### 4.4 Results

The optimized mass model and critical lines predicted by the model at  $z = 3.24$  are presented in Figure 7. We have used the two different common scaling relation and also included the gas measured using X-rays. For our best models we find  $\text{rms}_{\text{FJ}} = 0.197$  for Faber Jackson relation,  $\text{rms}_{\text{FP}} = 0.202$  for Fundamental Plane + Tully-Fisher and  $\text{rms}_{\text{X1}} = 0.158$  and  $\text{rms}_{\text{X2}} = 0.162$  for Fundamental Plane + Tully-Fisher + X-rays (X1 and X2) (see Figure 7 and 8 and Table 4).

Clearly, the influence of scaling relation on overall cluster mass model is minor, the fit of the model to the data seems to be very similar for both scalings, however it might be important for future detailed studies of galaxy clusters e.g. cluster lensing cosmography (Jullo et al. 2010; D'Aloisio & Natarajan 2011).

However, the rms of the model with explicitly included X-rays gas is better than without gas. The different gas mass distribution, derived with two different methods seems not to have a significant effect on the model fitting ( $\text{rms}_{\text{X1}}=0.158''$  vs.  $\text{rms}_{\text{X2}}=0.162''$ ). This is most probably due to the flexibility of the DM model. Apparently, the influence of gas mass is small enough that the model can compensate it by changing slightly the parameters of DM halos (position, ellipticity and size) without loosing precision of the multiple images position reconstruction. Nevertheless, including well measured gas mass is clearly a logical choice and does improve the rms of the model. This is especially important in case of the Bullet Cluster where DM and gas are spatially separated.

The evidences reported in Table 4 correctly summarize these observations. According to Jeffreys (1961), the difference between two models is substantial if  $1 < \Delta \ln(E) < 2.5$ , strong if  $2.5 < \Delta \ln(E) < 5$  and decisive if  $\Delta \ln(E) > 5$ . Following this criteria, there is a strong evidence that model with Xray is better than those without.

In Figure 7 we show the F606W-band image of the Bullet Cluster along with the contours generated from the projected mass map inferred from the best-fit model. This mass map is found to be in very good agreement with the light distribution. We find that the mass distribution of the Bullet Cluster consists of three dark matter clumps, the main clump of the Bullet Cluster is bimodal, which is in agreement with previous models of the Bullet Cluster. We find that DM1 and DM2 have high ellipticity and DM1 is comparable in mass to DM2 (see Table 4).

Furthermore, the galaxies and dark matter distributions share comparable centroid position, orientation and ellipticity. The agreement is a proof of the collisionless nature of dark matter, as suggested from the Bullet Cluster by Clowe et al. (2006). By integrating our two dimensional mass map,

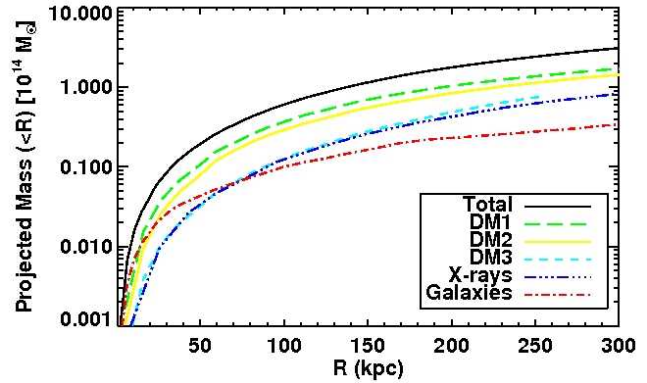


**Figure 8.** Total projected mass as a function of aperture radius centered at BCG1 (for the simplicity of the comparison with results of Bradač et al. 2006) for different model components. The two large scale clumps, DM1 and DM2, contribute a similar amount to the mass, the X-rays gas mass measured by (Markevitch et al. 2004) is  $\sim 9 \pm 3\%$  to the total mass at 250 kpc radius. The galaxies (including the BCG) contribute  $11 \pm 5\%$  within a 250 kpc radial aperture.

we get the total mass profile shown in Figure 8. In Figure 7 we compare also the mass profiles derived by TF relation and FP relation by plotting the critical lines of the two models corresponding to  $z=3.24$ , showing good agreement of these models.

We also compare the mass associated with the individual galaxies ( $M_{\text{galax}}$ ) together with the 3 BCGs to the total mass ( $M_{\text{tot}}$ ) as a function of radius (see Figure 9). Inside radius  $R = 250\text{kpc}$ , we find  $M_{\text{tot}} = 2.5 \pm 0.1 \times 10^{14} M_{\odot}$ , we find also that the contribution of the galaxy halos to the total mass is  $11 \pm 5\%$  at 250 kpc. As shown in the Figure 9 this fraction increases towards the center of the cluster, similar results were also observed in by Kneib et al. (2003); Limousin et al. (2007b).

We estimated the redshifts of the new candidate systems using the model predictions.

The estimated redshifts are reported in Table 2. A summary of the best-fit values inferred through the strong lensing optimization are reported in Table 4.

Finally, we have looked at the difference between A and B galaxies, and BCGs and the other cluster members using the measured and inferred properties  $V_{\text{disp}}$  and  $R_{\text{eff}}$ . We found that  $\langle V_{\text{disp}} \rangle = 100 \pm 28 \text{ km s}^{-1}$  and  $\langle R_{\text{eff}} \rangle = 56 \pm 14 \text{ kpc}$  for galaxy member, and also we find that out of the 82 elliptical galaxies in the catalog 35 are with  $V_{\text{disp}} < 100 \text{ km s}^{-1}$ . One of the two galaxies that has been separately modeled (galaxy A) have the two properties within the average galaxy member distribution  $V_{\text{disp}} = 101 \pm 5 \text{ km s}^{-1}$  and  $R_{\text{eff}} = 43 \pm 2 \text{ kpc}$ , while the velocity dispersion of the galaxy B is bigger than average galaxy member by  $79 \pm 37\%$  (see Figure 6).

## 5 CONCLUSIONS

The Bullet Cluster due to its rare characteristic (spacial separation of X-ray gas and rest of the matter) is an object of great interest for fundamental physics. The detailed study of its total mass distribution not only brings answers about



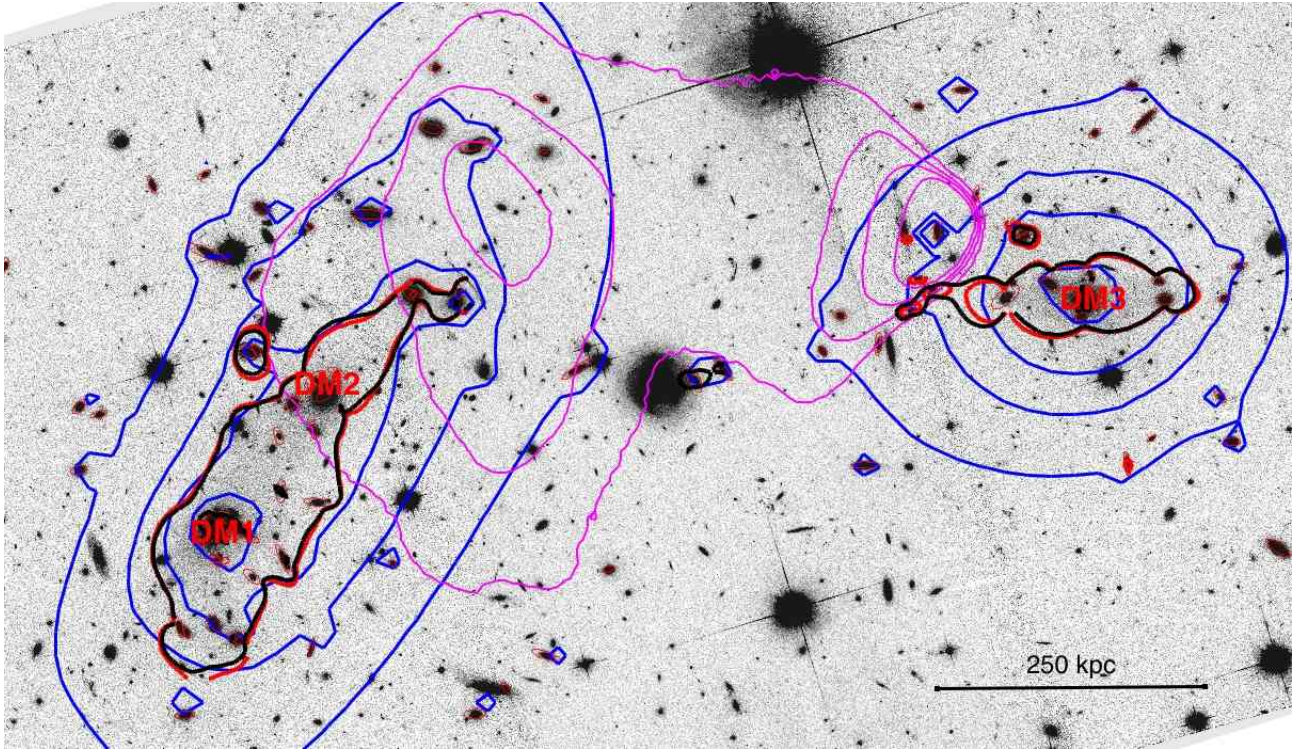


**Figure 7.** F606W-band image of the Bullet Cluster. The size of the field of view is  $150'' \times 250''$ . The blue contours show the projected mass density. The red line represent a critical line calculated using Faber-Jackson scaling relation to all cluster members while black line represents the result from use of the two scaling relation Fundamental Plane to ellipticals and Tully-Fisher for spirals. The magenta lines represent the contours of the Chandra X-rays brightness map.

existence and nature of dark matter but also provides an exceptionally strong gravitational telescope.

In this work we have reconstructed a mass map of the galaxy cluster 1E 0657-56 using strong lensing constraints and X-rays data. Using deep, high-resolution optical data we have revised the previously known multiple imaged systems and identify new ones. As a result our model is based on 14 multiply imaged systems with 3 spectroscopic redshifts. The model was sampled and optimized in the image plane by a Bayesian Monte Carlo Markov chain implemented in the publicly available software LENSTOOL. Our main conclusions are as follows:

1. Using the strong lensing mass reconstruction we derive a high-resolution mass map; we get a projected, enclosed mass  $M_{\text{main}}(< 250\text{kpc}) = 2.5 \pm 0.1 \times 10^{14} M_{\odot}$  and  $M_{\text{sub}}(< 250\text{kpc}) = 1.7 \pm 0.2 \times 10^{14} M_{\odot}$ . The main and sub clump masses are respectively  $(11 \pm 4)\%$  and  $(27 \pm 12)\%$  smaller to those predicted by (Bradač et al. 2006).
2. We have presented the implementation of the Fundamental Plane as a cluster members scaling relation and X-rays gas mass maps into the strong lensing mass modeling.
3. We have found, in agreement with previous models of 1E 0657-56 that the major mass component (cluster scale-DM halos) is in spatial agreement with the galaxies and not with the X-rays gas, which confirms the collisionless nature of dark matter. We detect the main and sub cluster DM peak being aligned with their BCGs, both clearly offset from the location of the X-ray gas in the system.
4. We have implemented the contribution of the X-ray

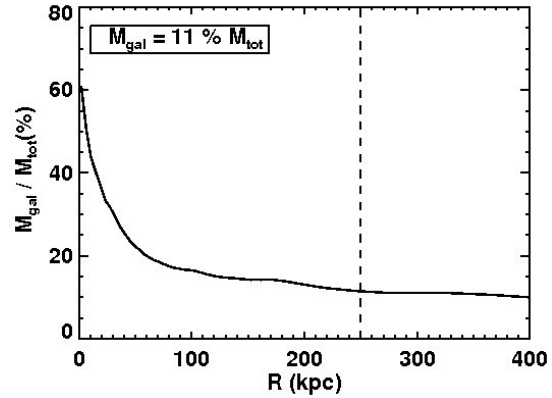


**Figure 9.** Contribution of the galaxy component to the total mass as a function of radius (centered on the BCG 1). The vertical dotted line shows the location of the 250 kpc radius where  $M_{\text{gal}} = 11 \pm 5\% M_{\text{tot}}$ .

gas mass in our mass modeling, which improved significantly the lensing rms model.

The high accuracy mass map we have presented is made available to the community and can be used to exploit 1E 0657-56 as a gravitational telescope, probing the high redshift universe (e.g. Kneib et al. 2004).

## ACKNOWLEDGEMENTS

JPK & ML acknowledges support from CNRS. JR acknowledges support from the EU Career Integration Grant 3DLENS and Dark Cosmology Centre. The Dark Cosmology Centre is funded by the Danish National Research Foundation. Data presented herein were obtained as part of programs 11591, 11099, 10863, 10200 from the NASA/ESA *Hubble Space Telescope*. Also partially based on European Southern Observatory program 084.B-0523 (PI: Mei). AM acknowledges support by Israel Science Foundation grant 823/09. This work received support from Agence Nationale de la Recherche bearing the reference ANR-09-BLAN-0234-01.

## REFERENCES

- Appenzeller I. et al., 1998, *The Messenger*, 94, 1
- Barrena R., Biviano A., Ramella M., Falco E. E., Seitz S., 2002, *A&A*, 386, 816
- Bekenstein J. D., 2004, *PhysRevD*, 70, 083509
- Bernardi M., Sheth R. K., Annis J., Burles S., Eisenstein D. J., Finkbeiner D. P., Hogg D. W., York D. G., 2003, *AJ*, 125, 1866
- Bertin E., Arnouts S., 1996, *A&AS*, 117, 393
- Boyarsky A., Ruchayskiy O., Markevitch M., 2008, *ApJ*, 673, 752
- Bradač M., Allen S. W., Treu T., Ebeling H., Massey R., Morris R. G., von der Linden A., Applegate D., 2008, *ApJ*, 687, 959
- Bradač M. et al., 2006, *ApJ*, 652, 937
- Bradač M. et al., 2009, *ApJ*, 706, 1201
- Clowe D., Bradač M., Gonzalez A. H., Markevitch M., Randall S. W., Jones C., Zaritsky D., 2006, *ApJL*, 648, L109
- Clowe D., Gonzalez A., Markevitch M., 2004, *ApJ*, 604, 596
- D'Aloisio A., Natarajan P., 2011, *MNRAS*, 411, 1628
- David L. P., Slyz A., Jones C., Forman W., Vrtilek S. D., Arnaud K. A., 1993, *ApJ*, 412, 479
- Djorgovski S., Davis M., 1987, *ApJ*, 313, 59
- Ettori S., 2000, *MNRAS*, 311, 313
- Faber S. M., Jackson R. E., 1976, *ApJ*, 204, 668
- Gerhard O., Kronawitter A., Saglia R. P., Bender R., 2001, *AJ*, 121, 1936
- Gonzalez A. H., Papovich C., Bradač M., Jones C., 2010, *ApJ*, 720, 245
- Halkola A., Seitz S., Pannella M., 2006, *MNRAS*, 372, 1425
- Jeffreys H., 1961, Oxford: Oxford Univ. Press
- Jullo E., Kneib J., Limousin M., Elíasdóttir Á., Marshall P. J., Verdugo T., 2007, *New Journal of Physics*, 9, 447
- Jullo E., Kneib J.-P., 2009, *MNRAS*, 395, 1319
- Jullo E., Natarajan P., Kneib J.-P., D'Aloisio A., Limousin M., Richard J., Schimd C., 2010, *Science*, 329, 924
- Kneib J., Ellis R. S., Smail I., Couch W. J., Sharples R. M., 1996, *ApJ*, 471, 643
- Kneib J. et al., 2003, *ApJ*, 598, 804
- Kneib J.-P., Ellis R. S., Santos M. R., Richard J., 2004, *ApJ*, 607, 697
- Koekemoer A. M., Fruchter A. S., Hook R. N., Hack W., 2002, in *The 2002 HST Calibration Workshop : Hubble after the Installation of the ACS and the NICMOS Cooling System*, S. Arribas, A. Koekemoer, & B. Whitmore, ed., p. 337
- Koopmans L. V. E., Treu T., Bolton A. S., Burles S., Moustakas L. A., 2006, *ApJ*, 649, 599
- LaRoque S. J., Bonamente M., Carlstrom J. E., Joy M. K., Nagai D., Reese E. D., Dawson K. S., 2006, *ApJ*, 652, 917
- Limousin M. et al., 2011, *ArXiv e-prints*
- Limousin M., Kneib J., Natarajan P., 2005, *MNRAS*, 356, 309
- Limousin M., Kneib J. P., Bardeau S., Natarajan P., Czoske O., Smail I., Ebeling H., Smith G. P., 2007a, *A&A*, 461, 881
- Limousin M. et al., 2007b, *ApJ*, 668, 643
- Limousin M. et al., 2008, *A&A*, 489, 23
- Markevitch M., 2006, in *ESA Special Publication*, Vol. 604, *The X-ray Universe 2005*, A. Wilson, ed., p. 723
- Markevitch M., Gonzalez A. H., Clowe D., Vikhlinin A., Forman W., Jones C., Murray S., Tucker W., 2004, *ApJ*, 606, 819
- Markevitch M., Gonzalez A. H., David L., Vikhlinin A., Murray S., Forman W., Jones C., Tucker W., 2002, *ApJL*, 567, L27
- Mehlert D. et al., 2001, *A&A*, 379, 96
- Milgrom M., 1983, *ApJ*, 270, 365
- Natarajan P., Kneib J., Smail I., Ellis R., 2004, *ArXiv Astrophysics e-prints*
- Natarajan P., Kneib J., Smail I., Ellis R. S., 1998, *ApJ*, 499, 600
- Natarajan P., Kneib J.-P., 1997, *MNRAS*, 287, 833
- Natarajan P., Kneib J.-P., Smail I., Treu T., Ellis R., Moran S., Limousin M., Czoske O., 2009, *ApJ*, 693, 970
- Neumann D. M., Arnaud M., 2001, *A&A*, 373, L33
- Nigoche-Netro A., Aguerri J. A. L., Lagos P., Ruelas-Mayorga A., Sánchez L. J., Machado A., 2010, *A&A*, 516, A96+
- Oguri M., 2007, *ApJ*, 660, 1
- Oguri M., 2010, *PASJ*, 62, 1017
- Ota N., Mitsuda K., 2004, *A&A*, 428, 757
- Peng E. W., Ford H. C., Freeman K. C., 2004, *ApJ*, 602, 705
- Pérez-González P. G. et al., 2010, *A&A*, 518, L15
- Randall S. W., Markevitch M., Clowe D., Gonzalez A. H., Bradač M., 2008, *ApJ*, 679, 1173
- Rex M., Rawle T. D., Egami E., Pérez-González P. G., Wilson G. W., Yun M. S., 2010, *A&A*, 518, L13
- Richard J. et al., 2007, *ApJ*, 662, 781
- Richard J., Kneib J.-P., Limousin M., Edge A., Jullo E., 2010a, *MNRAS*, 402, L44
- Richard J., Pei L., Limousin M., Jullo E., Kneib J. P., 2009, *A&A*, 498, 37
- Richard J. et al., 2010b, *MNRAS*, 404, 325
- Suyu S. H., Halkola A., 2010, *A&A*, 524, A94
- Tucker W. et al., 1998, *ApJL*, 496, L5+
- Tully R. B., Fisher J. R., 1977, *A&A*, 54, 661
- Vikhlinin A., Kravtsov A., Forman W., Jones C., Markevitch M., Murray S. S., Van Speybroeck L., 2006, *ApJ*, 640, 691